

Tectonics of Cerberus Fossae unveiled by marsquakes

Received: 19 March 2022

Accepted: 7 September 2022

Published online: 27 October 2022

 Check for updates

Simon C. Stähler¹✉, Anna Mittelholz¹, Clément Perrin¹, Taichi Kawamura¹, Doyeon Kim¹, Martin Knapmeyer¹, Géraldine Zenhäusern¹, John Clinton¹, Domenico Giardini¹, Philippe Lognonné¹ and W. Bruce Banerdt⁶

The InSight mission has measured the seismicity of Mars since February 2019 and has enabled the investigation of tectonics on the surface of another planet for the first time. Its dataset shows that most of the widely distributed surface faults are not seismically active, and that seismicity is mostly originating from a single population of tectonic structures, the Cerberus Fossae. We show that the spectral character of deeper low-frequency marsquakes suggests a structurally weak, potentially warm source region consistent with recent magmatic activity at depths of 30–50 km. We further show that high-frequency marsquakes occur distributed along the Cerberus Fossae, in the brittle, shallow part, potentially in fault planes associated with the graben flanks. Together, these quakes release an annual seismic moment of $1.4\text{--}5.6 \times 10^{15} \text{ N m yr}^{-1}$ or at least half the seismicity of the entire planet. Our findings confirm that the Cerberus Fossae represents a unique tectonic setting shaped by current day magmatic processes and locally elevated heat flow.

Faults are widespread and common on the Martian surface^{1,2}, providing evidence for brittle deformation throughout the planet's history. Owing to the lack of recent widespread volcanism, plate tectonics or high erosion rates that recycle the surfaces of Venus or Earth, Martian faults are well preserved over billions of years and do not necessarily correlate with recent tectonic deformation. The InSight mission landed on Mars to observe current day seismicity and thus tectonic activity using a broadband seismometer^{3,4}. Around InSight's landing site⁵, wrinkle ridges and lobate scarps, interpreted as buried reverse faults resulting from compression, are widely spread, with clusters in the large Isidis and Hellas impact basins, but also in the plains of Hesperia, Arcadia and Amazonis (Fig. 1). Their abundance in terrain of all ages was interpreted as the result of secular cooling and associated shrinking of the planet⁶, in combination with the weight of the large Tharsis volcanic region 6,000 km to the East⁷. Normal faults, that is extensional tectonic structures, are oriented radial to Tharsis (Extended Data Fig. 1). Westward, these are the 10–20 million years (Ma) old Cerberus Fossae⁸ in Eastern Elysium Planitia, and further southward

the much older Memnonia and Sirenum Fossae⁹. Based on the distribution of young faults in both Amazonis and Elysium Planitia (Fig. 1), one might therefore expect widespread seismic activity northeast of the InSight landing site, and nearby in all directions. However, the first seismic data from InSight's seismometer, SEIS (Seismic Experiment for Interior Structure), revealed a different picture.

The most significant marsquakes during InSight's first Martian year of operations (observed on Sols 173 and 235 of the mission, thus named S0173a and S0235b) were located at the approximate distance and in the direction of the Cerberus Fossae^{10,11}. Analysis of seismic waveforms showed that source mechanisms of both events are consistent with an extensional setting¹², suggestive of ongoing opening of the Cerberus Fossae. Until 31 March 2022, 22 out of 29 low-frequency (LF) marsquakes for which a location could be determined have been located at very similar distances, consistent with the Cerberus Fossae^{13–15} and, for seven of those, a focal mechanism could be determined, generally extensional¹⁶. LF quakes are similar in character to earthquakes, with clear P and S waves, and they are thought to occur in the lower crust or

¹Institute for Geophysics, ETH Zurich, Zürich, Switzerland. ²Department of Earth and Planetary Sciences, Harvard University, Cambridge, MA, USA.

³LPG-OSUNA, Nantes Université, Nantes, France. ⁴Institut de physique du globe de Paris, Université Paris Cité, Paris, France. ⁵Institute for Planetary Science, DLR, Berlin, Germany. ⁶Jet Propulsion Laboratory, California Institute of Technology, Pasadena, CA, USA. ✉e-mail: mail@simonstaehler.com

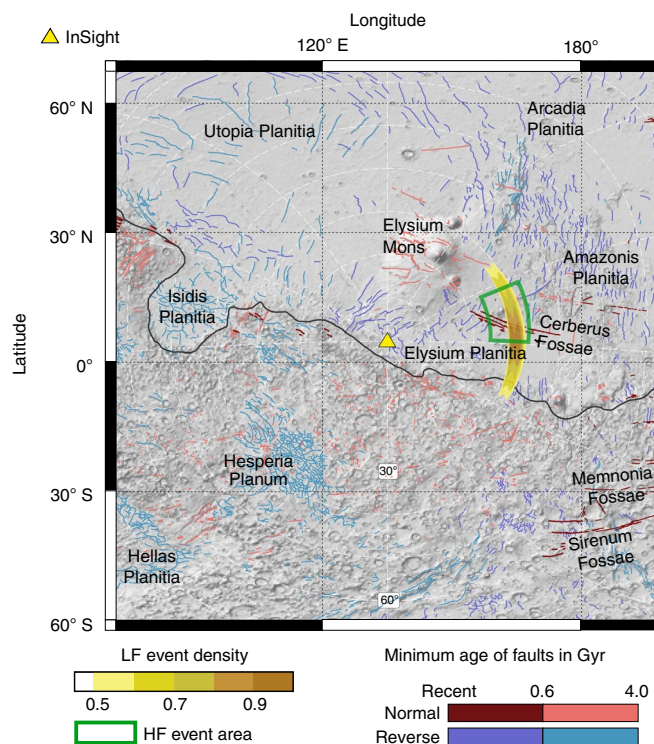


Fig. 1 | Faults around InSight. Faults and major geographic features in the InSight hemisphere colour-coded by age, grouped into normal and reverse faults^{1,21}. The yellow shaded area marks the normalized density of LF quakes^{14,31}. The green box highlights the back-azimuth range found by our analysis for HF marsquakes, corresponding to the dashed line in Fig. 3 and the distance range in which 80% of HF seismicity is present. Background shading: Mars Orbital Laser Altimeter (MOLA) topographic map⁷⁶. A global version of this map is available as Extended Data Fig. 1.

uppermost mantle¹¹, between 15 and 50 km depth^{12,17,18}. A second class of marsquakes is termed high-frequency (HF) events, owing to significant signal energy above 2 Hz (ref. ¹³). A long signal duration is interpreted as the result of a shallow hypocentre of less than a few kilometres depth, which creates reverberations of seismic waves in shallow subsurface layers¹⁹. HF events have been detected in much larger numbers, 1,150 until 31 December 2021, yet they have smaller magnitudes than LF events; their distance is clustered around 1,500 km and, because of a lack of clear polarization, their direction as seen from the lander has not been determined. Thus no tectonic explanation has yet been provided for this most common type of Martian seismicity. Here we determine the direction of HF events and corroborate the unique tectonic setting of the Cerberus Fossae system. We investigate the source character of LF events, which indicate a warm source region at depth as opposed to the brittle and shallow source region of HF events. Combining all information from both event classes allows us to derive a consistent picture of the tectonics in the Cerberus Fossae system.

So far, no other tectonic feature on the InSight hemisphere of Mars has been unequivocally confirmed to be seismically active¹³, and only recently, on Sol 976 (1 September 2021), InSight detected large marsquakes on the far side, in the Southern Tharsis province²⁰. Since no marsquakes at all have been clearly localized on wrinkle ridges or lobate scarps, that is contractional features, the Cerberus Fossae offers unique insight into Mars’s tectonics as a whole.

Geological context

The Cerberus Fossae system is approximately 1,200–2,300 km (20–40°) east of the InSight lander (Fig. 2b,c). It has been described

as a dyke-induced graben system^{21,22}, or a system of collapsed and widened volcanic fissures^{23,24}; we will refer to it as a system of fossae, which is a descriptive term for elongated depressions on Mars. The Cerberus Fossae consists of five main graben features (G1–G5 in Fig. 2b) trending northwest to southeast and between 250 and 600 km long, but further segmented. The smallest segments that can be identified on the surface are 5–10 km long²¹. The western-most fossae are more mature (that is, with larger width and throw) and well being connected, as opposed to the slightly connected segments at the eastern fossae²¹. The Cerberus Fossae was previously identified as the location with most recent volcanic activity on Mars² dated to less than 10 Ma (ref. ²⁵), contemporary with the deposition of surficial basalt deposits over Eastern Elysium Planitia^{8,26}. Moreover, a symmetric mantling deposit in the central part of the fossae has been identified²⁷, the Cerberus Mantling Unit (CMU; Fig. 2d), and it has been hypothesized that those are pyroclastic deposits younger than 200,000 years (ka). Large-scale radially extensional and concentrically contractional faulting (see the global fault map in Extended Data Fig. 1) from the topographic load of the Tharsis volcanic province would create the extensional stress field in the northwest direction in Eastern Elysium Planitia^{7,28}. The actual fracturing in the specific location could be due to weakening of the crust due to partial melting below Elysium Mons and a dyke system extending from there^{29,30}.

Marsquake hypocentre locations

Figure 1 shows the combined probability density of all LF quake locations including distance and direction using recently obtained back-azimuth estimates³¹ and velocity models³², and it peaks around Cerberus Fossae. The uncertainty in the back azimuth results in a relatively large geographical spread in the north–south direction. However, given that the distance spread (in the east–west direction) of the observed marsquake cluster is small, it can a priori be assumed that their north–south spread is of similar magnitude, allowing us to place all of these events into the Cerberus Fossae. The five segments of the Cerberus Fossae grabens (G1–G5) are concentrated in two main regions²¹, where G1, G2 and G3 are in a distance range of 18–27 from InSight, while G4 spans the range of 33–39°. G5 is more faint, less mature and bridges the two main regions. The graben strike is 15° off the direction of the lander. Distance differences of LF events can most easily be explained by different locations along the fossae. To identify such locations, we evaluate if the event cluster is consistent with certain locations along the fossae (Fig. 2a,b) when varying the seismic velocity models. In the ‘near’ end-member model, the cluster of events would occur at the eastern end of G1 or in G5. In the ‘far’ case, it would be placed on G5 and G4. A single event, S0325a¹³ would be located at the eastern end of G4 (not shown in Fig. 1), but given that this event has a poorly determined back azimuth³¹, it cannot be clearly attributed to the Cerberus Fossae. We conclude that the majority of localized LF events on the InSight hemisphere cluster in the central Cerberus Fossae (Fig. 1).

Localizing HF events has not been attempted at all so far because of the strong scattering and the lack of ballistic arrivals¹⁹. We realign the events to better constrain relative distances (Extended Data Fig. 2) and stack horizontal component envelopes. We find a surplus of energy in the $78 \pm 12^\circ$ back azimuth around the P-wave arrival, consistent with a source in the direction of the Cerberus Fossae (Fig. 3 and Extended Data Fig. 3). We further examine their distance distribution and while it is broader than that of the LF events, we find that it indeed matches the extent of the Cerberus Fossae (Figs. 1 and 2a). Thus, we can plausibly assume that shallow HF seismicity also originates in the Cerberus Fossae. The HF sources are spread over a large part of the Fossae, as opposed to the more focused distribution of deeper LF events.

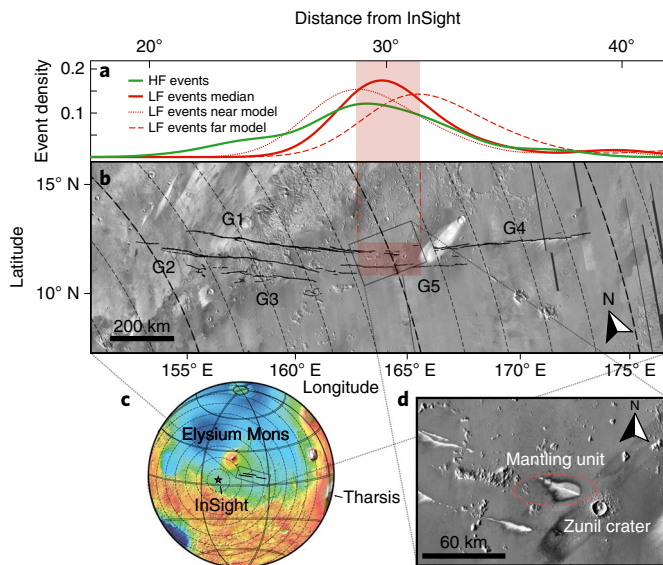


Fig. 2 | Seismicity at Cerberus Fossae. **a**, Density of seismic moment release along the profile of the Cerberus Fossae. Probability density functions from a Gaussian kernel density estimation of HF (green) and LF (red) moments are shown separately. For the LF events, three candidate distributions based on different mantle models are shown (the median model is shown in Fig. 1). The red box highlights the area between near and far model peaks in **a** for easier comparison with **b**. **b**, Oblique Mercator projection of Mars Odyssey's Thermal Emission Imaging System (THEMIS, day-time infrared) highlighting the five main graben features G1–G5 of the Cerberus Fossae (mapping from ref. ²¹). Dashed lines indicate the distance to InSight with bold lines indicating 20°, 30° and 40°. **c**, MOLA topography inset for global context and 10° distance circles around InSight. **d**, The area of highest marsquake density; the Cerberus Mantling Unit (CMU recently identified as a volcanically active feature in ref. ²⁷) is circled.

Seismic moment

Estimating seismic moment release

Marsquake Service (MQS) routinely estimates magnitudes³³ and their uncertainties. For LF events, the magnitude uncertainty takes into account the distance uncertainty and the error in estimating the long-period amplitude³³. Identification of marsquakes is limited to times of low wind at InSight, which make up approximately one third of the total duration averaged over the mission^{13,34}. When estimating the total seismic activity rate of a region, one needs to take into account not only the detection probability due to wind noise, but also the inherent randomness of the number of events per year. A Monte Carlo method has been proposed³⁵ to estimate the likelihood for annual moment release and maximum event size, given a short and incomplete catalogue. Following this procedure, we estimate the total annual moment rate in the Cerberus Fossae to be $1.4\text{--}5.6 \times 10^{15} \text{ N m yr}^{-1}$ (Extended Data Figs. 4 and 5). Regarding Mars's seismicity as a whole, SEIS observed a total of 45 LF marsquakes on the InSight hemisphere rated as quality A, B or C (A–D is highest to lowest, where D is unlocatable) up to 31 March 2022¹⁴. Six of them are unequivocally located outside the Cerberus Fossae, compared to 17 in the Cerberus Fossae. The remaining 22 cannot be located due to noise. Thus, from the observations so far, the small region of the central Cerberus Fossae accounts for at least half of the seismic moment release of the whole InSight hemisphere.

Seismic versus geological deformation

Following the morphological estimate of ref. ²⁵, the formation of the Cerberus Fossae grabens G1–G4 requires deformation equivalent to a seismic moment of $M_{0,\text{total}} = 2.1 \pm 0.5 \times 10^{24} \text{ N m}$, assuming a constant rate \dot{M}_0 since the opening 5–20 Ma, $\dot{M}_0 = 0.5 – 2.2 \times 10^{17} \text{ N m yr}^{-1}$. This prediction exceeds our seismic observation by a factor of 50 and is a

first indication that the current seismicity rate is not representative of the entire formation process.

Next, we focus on the observed seismicity cluster which spreads over a distance of 400 km and a range of ~20 km in depth (thus providing an area A). Using a shear modulus of $\mu = 24 \text{ GPa}$ (ref. ³⁶) and assuming that all of the seismicity was extensional, the observation is equivalent to a slip rate of $\dot{s}_{\text{seism}} = \frac{M_0}{\mu A} = 7 – 30 \times 10^{-6} \text{ m yr}^{-1}$. For G1 and G2, the geological deformation rate is $\dot{d}_{\text{geol}} = 5 – 73 \times 10^{-5} \text{ m yr}^{-1}$ (ref. ²⁷). The central young CMU (53–210 ka; ref. ²⁷) shows a throw of at least 100 m, equivalent to a slip rate of $\dot{s}_{\text{geol}} = 5 – 20 \times 10^{-4} \text{ m yr}^{-1}$ over the last few 10 ka, assuming continuous deformation. The current seismic slip rate \dot{s}_{seism} explains only 1–10% of the total deformation, d_{geol} , preserved in the geological record.

The shallow seismicity associated with the HF events is at least a factor of 10 below the LF events because of their smaller magnitudes and it is distributed over a larger area. It can therefore not explain the discrepancy between geological deformation and observed seismicity.

A case for dyke-induced tectonic activity in the source region

Spectral characteristics

The duration of a quake, whether on Earth or Mars, places a limit on the coherent HF seismic energy radiated from it. This is typically expressed via the corner frequency in the source spectrum, f_c , above which the displacement amplitude, $A(f)$, decreases as f^n , where $2 < n < 3$ (ref. ³⁸). For all investigated LF events in the Cerberus Fossae, we find that $0.45 < f_c < 0.95 \text{ Hz}$ (Extended Data Figs. 6 and 7). As shown in Fig. 4c, this is significantly less than the values found empirically for $M_W \approx 3$ earthquakes^{39,40}, which is 2–10 Hz. In comparison, LF marsquakes outside the Cerberus Fossae, specifically a recent marsquake in Syrtis Major Planum, S1102a (2 January 2022, Fig. 4b), but also other events at distances of 3,000–4,000 km (red stars in Fig. 4c) show significantly higher values of $f_c > 1.5 \text{ Hz}$. The corner frequency of the shallow HF events is significantly higher (Fig. 4b). For the largest HF events, a roll-off in displacement spectrum is observed above 3 Hz. Given the unknown crustal attenuation, this puts only a lower limit on f_c . For magnitudes $1.5 < M_W < 2.5$, f_c is still at the low end of terrestrial quakes, although the uncertainty both on magnitude and f_c is high.

A feasible explanation for the observation of ‘slow’ quakes is a reduced shear wave velocity, β , in the source region, because in classic models f_c scales linearly with β (ref. ³⁸), that is,

$$f_c \propto \beta^3 \sqrt{\Delta\sigma/M_0} \quad (1)$$

where $\Delta\sigma$ is the stress drop. InSight observed low β of $1.3\text{--}1.8 \text{ km s}^{-1}$ in the uppermost 10 km below the lander as derived using receiver functions^{10,36} and autocorrelations⁴¹, which is a factor of ~2 below the value in terrestrial crustal models (for example, ref. ⁴²). If the hypocentres were located within this layer, this could explain a factor of 2 in corner frequency compared with the bulk of terrestrial crustal earthquakes, but hardly the observed factor of 5–10. Also, so far all published results agree on LF event depths of at least 15 km (refs. ^{12,17,18,43}), where β is comparable to terrestrial values.

Local weakening, for example due to warmer materials near a dyke in the source region, could present a second effect leading to the observations. The stress drop ($\Delta\sigma$ in equation (1)) describes the difference of the shear stress on the fault plane before and after the quake. It can be derived analytically for simple fault geometries in homogeneous media, and otherwise represents an empirical term⁴⁴. As a general rule, low values for f_c and thus $\Delta\sigma$ are found in volcanic settings, where material is heated and close to ductile behaviour⁴⁵. This would require the hypocentres to be located in a zone of increased temperature, possibly close to a magma chamber feeding shallower

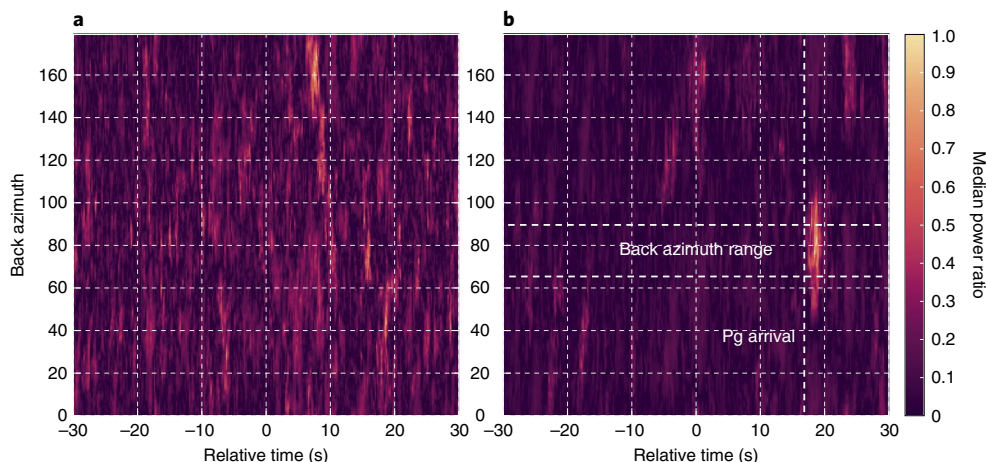


Fig. 3 | HF event localization. **a,b,** The energy ratio between the radial and transversal horizontal components for the HF envelope stack (**a**) before and (**b**) after re-alignment (Methods). The energy maximum at a back azimuth of

$78^\circ \pm 12^\circ$ (dashed lines) corresponds to P-wave energy from the central part of the Cerberus Fossae. The time axis is relative to an arbitrary offset used before alignment, the Pg arrival is thus marked.

dykes (Fig. 5). This explanation is consistent with the depth estimates for LF and HF events. The deep LF events are closer to the weakening heat sources and thus show a slower rupture process than the shallower and slightly faster HF events.

A third possible explanation could be that the lower gravity on Mars reduces yield strength and could thus lead to generally lower stress drops and therefore f_c . However, shallow moonquakes show even higher f_c values⁴⁶ and large marsquakes outside of the Cerberus Fossae have significantly higher f_c , falling within the range expected for terrestrial quakes (the red line in Fig. 4b). This observation confirms that the discussed events are different and highlights the Cerberus Fossae's unique setting.

Recent volcanism in the Cerberus Fossae

The CMU near Zunil Crater has been hypothesized as being a recent product of explosive volcanism²⁷, based on the symmetric distribution of material and decreasing thickness with distance from the source fissure (Fig. 2d). The dust and streaking directions overlay that of the Zunil Crater itself, dated at 0.1–1 Ma. While the hypothesis of explosive volcanism may be unproven, the detailed age estimates of the CMU of 53–210 ka, make it one of the youngest features mapped on the Martian surface to date²⁷. Because there is no sign of younger volcanism locally, the structure would have to be considered dormant or inactive.

Terrestrial volcanoes of this age can still be in an active state with ongoing fluid motion identified by seismic activity⁴⁷. The observation of marsquakes around the CMU is thus intriguing and we compare our observations with two categories of seismic activity near dormant volcanoes on Earth (for an overview, see, for example, ref. ⁴⁸): (1) deep low-frequency events (DLEs), which are ‘slow’ quakes of magnitudes <2. These events typically occur in swarms, that is week-to-year-long activity bursts; (2) volcanic tremor, long-duration, monochromatic signals.

In comparison, our studied events on Mars do not quite match any of these two categories. While martian LF events are abnormally slow, they do not qualify as DLEs, because they are too large in magnitude (which would require very significant subsurface magma motion). Moreover, their recurrence rate also shows no deviation from a stationary Poisson process (Extended Data Fig. 8), unlike DLEs, which occur in swarms. We note that at distances of 1,500 km or more the seismometer lacks the resolution to observe very slow events, including DLEs below magnitude 2.5 (the region below the red line in Fig. 4). We therefore cannot rule out signals from fluid motion, but discussed event observations are not consistent with Earth-like DLEs. Others⁴⁹ have investigated whether several LF marsquakes could be explained

by volcanic tremor, but found that, for the magnitude and spectral content, very large magma flow rates over short time windows would be needed. This is in apparent contradiction to the low number of marsquakes observed so far and the lack of surficial expressions of current active volcanism. Also, the events discussed in this study show very clear P- and S-wave arrivals, unlike the more emergent signals of tremor on Earth. In summary, we do not find evidence of tremor or generally fluid motion in the seismic data.

Inferred rupture size

Last, under the assumption of a circular source, f_c allows us to infer the source radius as $r = 0.38 \frac{\beta}{f_c}$ (ref. ⁵⁰). Within the range of β between 2 and 3 km s^{-1} , we obtain rupture plane radii of 1,200–1,800 m. This is below the minimum size of mapped surface segments within the Cerberus Fossae grabens (5–10 km; ref. ²¹), suggesting that small to moderate size marsquakes are not primarily limited by fracture geometry and that over longer observation times significantly larger marsquakes could occur, compatible with the large, potentially co-seismic boulder avalanche traces observed in orbital imaging⁵¹. The shallower HF quakes probably happen in the uppermost, low- β layer³⁶, with source radii between 150 and 300 m.

Discussion of the evolution of the Cerberus Fossae

Seismic data confirm ongoing opening of the Cerberus Fossae on Mars. Seismicity at 15–50 km depth with slow rupture processes suggests an extensional stress regime located in a warm source region.

The east–west distribution of events shows focused seismic activity in the centre of the Cerberus Fossae with generally low current seismicity probably opened rapidly and became mostly passive after a short time, as commonly observed for volcanic fissures. If the seismicity of the central event cluster is related to the CMU, this is consistent with rapid opening of a fissure 53–210 ka, as observed for dyke-induced fractures on Earth⁵². Nevertheless, the fact that we do not see LF seismicity in most parts of the Cerberus Fossae, specifically in the fractured western part where the largest deformation can be found, suggests a dynamic process that ceases after an initially active phase and might continue to propagate eastward.

We propose that the shallow seismicity from HF events is created by ruptures at shallow depth due to the graben structure itself, possibly the subsurface continuation of the graben flanks (Fig. 5). The rapid rupture associated with these quakes is not consistent with sources such as landslides or other mass wasting processes. More likely it is caused by the release of residual stress. A modulation of the HF quake

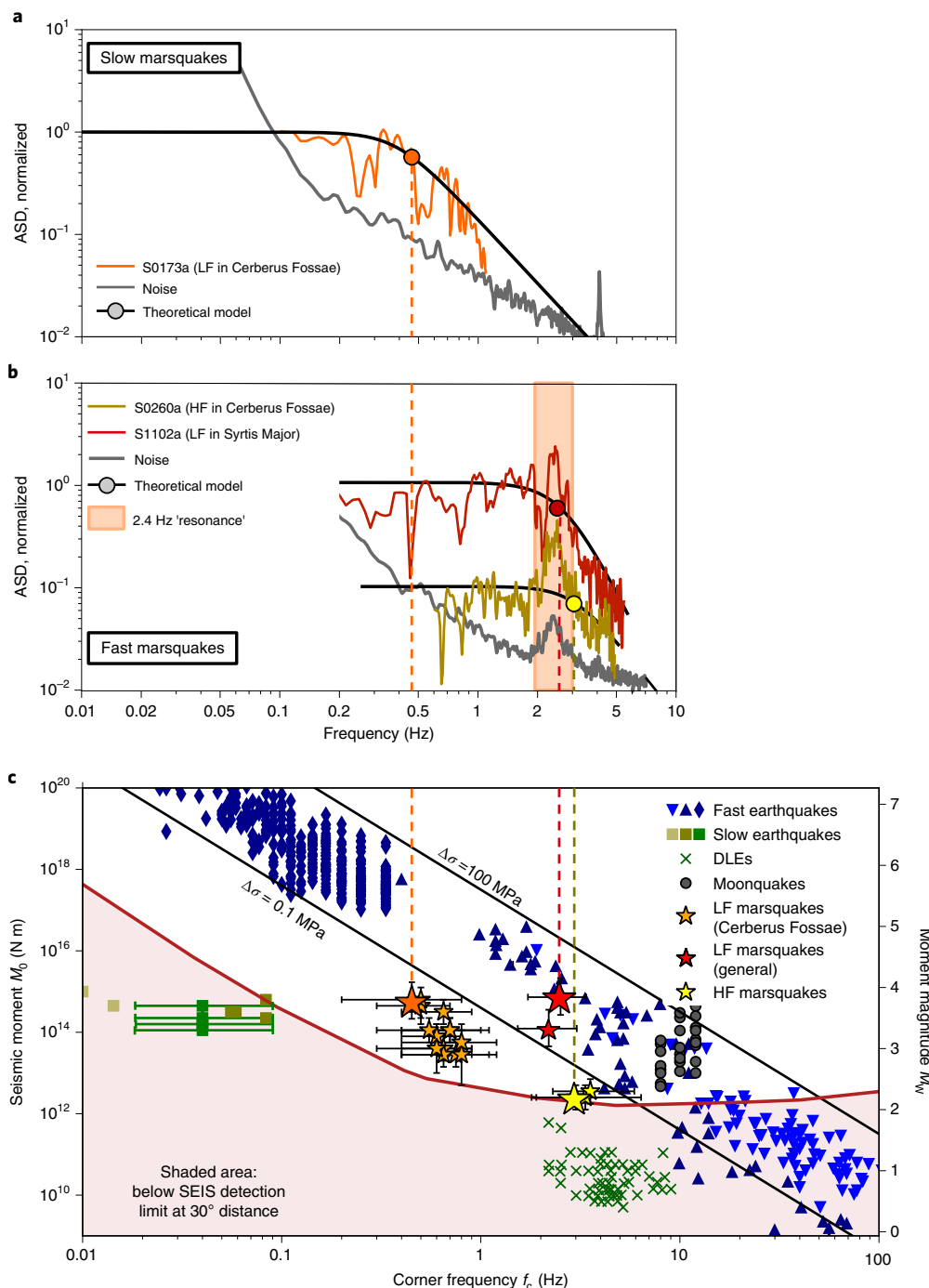


Fig. 4 | Spectra of marsquakes and source parameters compared to terrestrial and lunar quakes. **a**, Source amplitude spectral density (ASD) of the Cerberus Fossae LF marsquakes S0173a. **b**, Source ASD for HF marsquake S0260a and distant LF marsquake S1102a. The source spectra were estimated from the vertical displacement P waveform, normalized and corrected for attenuation, assuming $Q_p=1,000$. The black solid lines show best fitting theoretical Brune source spectra with exponent $n=2$ or 3, and corner frequency f_c marked by the circles. The background noise curves in **a** and **b** are from data before the P-wave arrival. The orange area in **b** is the local '2.4 Hz' subsurface resonance described in refs. ^{77,78}. **c**, Seismic moment M_0 versus corner frequency f_c for different types

of quakes observed on the Earth, the Moon and Mars. Blue symbols mark regular, 'fast' earthquakes, following a cube law between seismic moment and corner frequency for three datasets of shallow earthquakes (in order of symbols left to right, refs. ^{39,79,80}). The brown squares mark a group of deep, slow events in Japan⁸¹, the green crosses mark slow events related to volcanism, observed in Germany⁴⁷; grey dots are fast shallow moonquakes⁴⁶. The error bars mark standard deviations from our analysis and the literature, where available. Black lines are f_c values for stress drops of 0.1 and 100 MPa for $\beta=3 \text{ km s}^{-1}$. LF marsquakes outside the Cerberus Fossae (red star) follow the $f_c \propto M_0^{-3}$ trend of earthquakes, whereas the Cerberus Fossae LF events specifically are significantly slower.

rate with a period of one Martian year was found³⁴ and its phase matches the peak solar elevation in equatorial latitudes. Given that significant parts of the Cerberus Fossae are deep enough to be in shadow over half of a Martian year, this is a plausible correlation and consistent

with shallow sources. However, a physical model connecting the two factors, illumination and quake rate, is still missing.

Globally, the clearly localized seismicity suggests that global contraction and therefore lithospheric compression are not the dominant

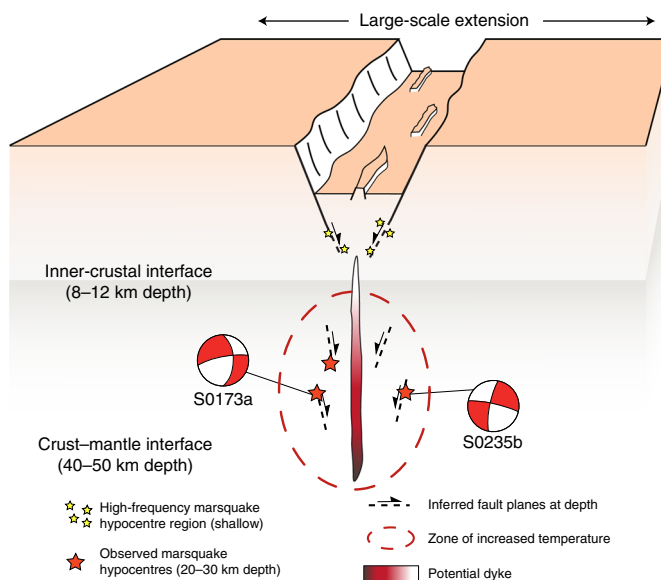


Fig. 5 | Vertical sketch of an active part of the Cerberus Fossae viewed from the east. The LF marsquake depths indicate faulting in the lower part of the crust and the low stress drop suggests that hypocentres (red stars) are located in the zone of increased temperature (red dashed) around a (recently) active dyke at depth. Event S0235b has been previously located to the north of the fault and S0173a to the south. In combination with the focal mechanisms (represented by ‘beachballs’ inferred in ref. ¹²), rupture planes dipping towards the dyke are plausible. In the shallow part, HF marsquakes are caused by residual stress on the flanks of the graben (yellow stars). The focal mechanisms are plotted as seen from the 70° azimuth, that is along the Fossae’s strike.

driver of contemporary tectonics on Mars. The Cerberus Fossae alone releases $1.4\text{--}5.6 \times 10^{15} \text{ N m yr}^{-1}$ seismic moment, a factor of 2–8 more than the Moon globally³⁵, where shallow seismicity has been identified on compressional faults⁵³. The slow character of the Cerberus Fossae events requires a warm source region. To be close to ductile rheology, a temperature of $1,000 \pm 100 \text{ K}$ is required for basaltic compositions^{54,55}. Assuming a quake depth of $40 \pm 10 \text{ km}$, this results in a local crustal thermal gradient of $20 \pm 2 \text{ K km}^{-1}$ in the Cerberus Fossae and a local heat flow of $36 \pm 10 \text{ mW m}^{-2}$ (assuming thermal properties of basalt⁵⁶). This is a factor of 1.7 above the global average values of $21 \pm 7 \text{ mW m}^{-2}$ and $22 \pm 1 \text{ mW m}^{-2}$ found by joint seismic and geophysical inversions^{43,57}. Such a localized high heat flow in Elysium has strong geodynamical implications. Either a dynamic heat source exists, such as a plume, or the partial melting results from locally thick crust. This in turn is difficult to reconcile with a thicker crust in the southern hemisphere, and therefore implies a low crustal density there³⁰.

The distribution and character of marsquakes show that the global stress field cannot exclusively explain the origin of the Cerberus Fossae. Instead, partial melting below Elysium probably weakens the crust locally and allows the grabens of the Cerberus Fossae to open. Across the solar system, a pattern emerges, where the present-day tectonics of the larger terrestrial planets, Mars, Venus and the Earth, is dominated by internal dynamics⁵⁸ instead of purely passive cooling and shrinking, as is found on the smaller Moon and Mercury.

Methods

Distance

Marsquakes are located by the MQS⁵⁹. Their respective distances from the InSight lander are determined from seismic data in combination with geophysically constrained velocity models, that is without taking previous tectonic information into account. For LF events, MQS uses the arrival time difference between P and S waves, the two strongest seismic body waves, to compute the distance of the event from InSight.

This travel time difference is compared with predicted travel times for a suite of inferred one-dimensional velocity-density structure models of Mars’s interior^{13,18,57}. The uncertainty in absolute distance is a combination of uncertainty in picking the arrival times and the span of possible seismic velocities in the interior model suite⁶⁰. The uncertainty in seismic velocities from most recent interior models is about 5%⁵⁷. If one separates the effect of pick uncertainty and velocity model uncertainty, the relative distances of all marsquakes can be determined with much higher precision than their absolute distances, allowing one to identify a cluster of seismic activity. The absolute distance of this cluster can then be estimated using different types of interior velocity models (Fig. 2a).

We use P- and S-wave pick times of the MQS catalogue version 9 (ref. ¹⁴) for marsquakes at distances within 3,000 km ($\approx 50^\circ$) of InSight and investigate the distance spread resulting from two end-member velocity models and one median model from ref. ³². The model with slowest/fastest velocities creates the set of near/far solutions. From these event distances, we determine a normalized seismicity density over distance (Fig. 2a). The uncertainty in depth of the events is estimated to be of the order of 20 km, and is reflected in the distance distributions.

For HF events, we use MQS S/P picks (termed Sg and Pg, due to crustal propagation¹³) and according to MQS practice we assume that the onsets of the two observed phases propagate with velocities of $v_{\text{Pg}} = 4 \text{ km s}^{-1}$ and $v_{\text{Pg}}/v_{\text{Sg}} = \sqrt{3}$ (ref. ¹³), consistent with velocities of the lower crust³⁶. The 286 HF events are spread over a distance range of 1,200–2,500 km (20–40°), with a clear maximum between 1,700 and 2,000 km (27° and 32°; Fig. 2a), consistent with the centre of the Cerberus Fossae (Fig. 2a).

Direction

Because InSight is a single station only, the direction towards an LF event (termed back azimuth) is estimated independently from the distance. MQS originally used the linearity of P-wave motion⁶⁰, which only resulted in direction estimates for eight events, due to the low signal-to-noise ratio (SNR). A recently proposed more robust alternative is based on the eigenvalues of the spectral matrix⁶¹ for P and S waves³¹. With this approach, we found that at least 14 events are located within 150 km north or south of the Cerberus Fossae as seen from InSight (Table 1). By application of the method to well-located terrestrial data of similar signal-to-noise ratio, it has been found³¹ that this is within the uncertainty of the method at a distance of 1,500 km. Therefore, all these 14 LF marsquakes are compatible with locations in the Cerberus Fossae (Table 1). Probability density functions for distance are computed as described above and back azimuth for LF events are taken from ref. ³¹. Figure 2 only shows distance distributions for all investigated events using different interior models and a mean model. In Fig. 1 we multiply the normalized mean distance and back-azimuth distributions.

The direction of HF events has so far been unknown, because the highly scattered first arrival has not shown an increased degree of polarization for any single event^{13,31}. Here we make use of the large number of HF events observed so far. To investigate whether the epicentres of the HF events are in a similar location, we stack all HF event waveforms and compare horizontal seismogram power in the radial direction of the central Cerberus Fossae (78° from north) with that in the orthogonal direction (transverse). If the sources are indeed located in this direction, we expect the P-wave arrival to show higher energy in the radial direction, at least in a short time window, in which ballistic waves dominate.

For this analysis, all MQS HF events with event quality C or above are used¹⁴. For each event, we use a standard algorithm of STA/LTA (short time average over long time average) triggering on the corresponding energy envelope averaged across all three seismogram components to pick Pg and Sg arrivals (hereby referred as the MQS picks, for example, refs. ^{11,13}). Here our energy envelope is computed for instrument-removed velocity waveforms in the spectral domain using a 30 s window with 90% overlap. We remove noticeable glitches and donks (see a detailed

Table 1 | Table summarizing marsquake parameters

Event	Quality	Distance (deg)	M_w	f_c	Back azimuth (deg)			
					MQS	Uncertainty	Pol.-based	Uncertainty
Events in the Cerberus Fossae								
S0173a	A	30.0	3.7 ± 0.3	0.45 ± 0.15	91	79–102	88	78–103
S0235b	A	28.7	3.7 ± 0.2	0.45 ± 0.15	74	66–88	77	64–100
S0802a	B	30.0	2.9 ± 0.2	0.75 ± 0.25	–	–	82	65–96
S0809a	A	29.8	3.3 ± 0.2	0.7 ± 0.3	87	67–105	91	82–100
S0820a	A	30.2	3.3 ± 0.2	0.55 ± 0.25	88	76–107	106	85–120
S0864a	A	28.7	3.1 ± 0.2	0.6 ± 0.2	97	83–116	90	66–110
S0916d	B	29.3	2.9 ± 0.2	0.95 ± 0.35	–	–	97	41–114
S1133c	A	30.2	3.8 ± 0.2	0.8 ± 0.2	–	–	90	70–110
Events likely in the Cerberus Fossae								
S0105a	C	32.5	3.0 ± 0.4	0.5 ± 0.2	–	–	112	95–133
S0325a	B	39.7	3.7 ± 0.3	0.5 ± 0.2	–	–	57	43–73
S0407a	B	29.3	2.9 ± 0.3	0.7 ± 0.2	–	–	57	43–169
S0409d	B	31.1	3.2 ± 0.3	0.5 ± 0.2	–	–	70	50–90
S0474a	C	29.1	2.9 ± 0.3	0.6 ± 0.2	–	–	97	72–123
S0484b	B	31.8	2.9 ± 0.2	0.6 ± 0.3	–	–	100	80–120
S0784a	B	34.5	3.3 ± 0.2	0.8 ± 0.3	–	–	115	92–136
Other marsquakes								
S1102a	A	74	3.6 ± 0.2	2.85 ± 1.0	286	261–309	22	354–355
S0185a	B	59.8	3.1 ± 0.3	1.8 ± 0.6	–	–	–	–

The marsquake events, type (BB, broadband), distance, M_w , quality (highest to lowest for A, B and C) and MQS back azimuths are taken from the MQS catalogue^{13,14}. Magnitude M_w and s.d. estimates are based on data from ref. ³⁴. Polarization (pol.) back-azimuth values and uncertainties are described in ref. ³². Events in italics have less certain back-azimuth estimates (see ref. ³²).

description of these electro-mechanical signals in, for example, refs. ^{62–64}) within our analysis window between the Pg and Sg arrival times. In addition, we discard those events for which spectral envelopes significantly deviate from the mean envelope of all HF event data. Therefore, 62 out of the 116 events with corresponding correlation coefficients <0.8 are not considered in the analysis. Next, the initial alignment guided by the MQS picks is refined for both Pg and Sg arrival times systematically using the implementation of a multichannel cross-correlation method⁶⁵ in order to obtain precisely aligned waveform data with our updated picks (Extended Data Fig. 2a,b). A pick uncertainty is assigned based on the duration of the amplitude rise time for each spectral envelope (starting from the onset until the amplitude reaches its maximum). Figure 2c shows the comparison of the relocated versus the MQS distance estimates with velocities of $v_{Pg} = 4 \text{ km s}^{-1}$ and $v_{Pg}/v_{Sg} = \sqrt{3}$. The observed difference in the two sets of distance estimates is small, with the mean and standard deviation of the MQS versus relocated distances being $24.7 \pm 2.9^\circ$ and $24.0 \pm 2.6^\circ$, respectively. To estimate the dominant direction of seismic energy travelling from the HF event cluster, we perform a grid search on back azimuths that maximize the median power ratio between the radial versus transverse component within –30 s to 30 s of the aligned Pg arrivals across multiple HF events simultaneously (for example, data bounded by the red lines in Extended Data Fig. 2a,b). A similar approach has been successfully applied to individual LF/broadband marsquake data in a recent receiver function analysis^{10,36,66}. Further, we apply a 2 s moving window to compute the power ratio at each time point for all 62 HF events and obtain the weighted median power ratio. In this process, we use relative weights for our HF events based on the signal-to-noise ratio of each individual event. The average background power ratio is estimated by (1) stacking those values computed within the pre-event noise window (that is, values between –30 s and 0 s) and (2) subtracting those from our resulting power ratios

(Extended Data Fig. 3). Our back-azimuth search on HF data aligned by the MQS picks did not show any prominent arrivals in the –30 s to 30 s search window (Extended Data Fig. 3a). However, we observe that the maximum power ratio is strongly focused at the back-azimuth value of $78 \pm 12^\circ$ once our events are systematically re-aligned (Extended Data Fig. 3a,b) despite a number of weak scattered maxima in the time window. Notably, energy arriving after ≈ 20 s becomes much more apparent when we repeat the analysis using a subgroup of HF events around a 24° distance, which forms the largest sample size within the central Cerberus Fossae event cluster (Extended Data Fig. 3c). The time axis in this plot is shifted arbitrarily due to the re-alignment.

Estimating total moment rate

Estimating the long-term average moment release rate from an incomplete catalogue is affected by the annual variability of moment release that even a perfectly Poissonian distribution of quakes shows.

We first test the distribution for deviation from a Poisson process, by plotting the cumulative count of events over time and the lag time between events (Extended Data Fig. 8) and while we find an increased rate in the second year, both years show no significant deviation from a Poisson process. For the annual rate, we follow the approach presented in ref. ³⁵ to estimate the parameters of a tapered Gutenberg–Richter size–frequency distribution⁶⁷: The cumulative number of earthquakes Φ above a magnitude M is then given by

$$\Phi(M) = \left(\frac{M_t}{M} \right)^\beta \exp \left(\frac{M_t - M}{M_c} \right) \quad (2)$$

where β is the slope of the power law, describing the distribution of larger to smaller quakes, M_c describes the magnitude above which the distribution tapers, that is larger events occur less often than expected

by the power law, and M_t is the magnitude of completeness of the catalogue. The total annual moment release \dot{M}_t can then be estimated from these parameters, as described in ref. ³⁵.

For the events observed in the Cerberus Fossae, we assume a slope $\beta = 2/3$, equivalent to a b value of 1 in the Gutenberg-Richter distribution. We use the KS_{10} estimator from ref. ³⁵ that uses the ten largest events of a catalogue with unknown M_c . We further need to take into account that only during 26% of the observation time were the local atmospheric conditions quiet enough to observe marsquakes. To account for magnitude uncertainty, the analysis was repeated 10,000 times with individual event magnitudes randomly varied according to their estimated uncertainty ³³ in the MQS catalogue version 9.

The resulting estimate of corner magnitude and moment rate are shown in Extended Data Fig. 4, using the KS_{10} estimator of ref. ³⁵, in the same style as in their Figures 4 and 7. The estimated long-term annual (a) moment rate is $2.93 \times 10^{15} \text{ N m a}^{-1}$, with an 80% interval between $1.35 \times 10^{15} \text{ N m a}^{-1}$ and $5.52 \times 10^{15} \text{ N m a}^{-1}$ (Extended Data Fig. 5).

Spectral character

Estimating the source spectrum of a quake is difficult from a single seismic record, because the high-frequency fall-off is affected by attenuation, both from intrinsic viscoelasticity, Q_i (refs. ^{68,69}), as well as scattering, Q_{scat} (ref. ⁷⁰). For frequencies above 1 Hz, scattering has been found to affect P and S waves considerably, on Earth ⁷¹ and on the Moon ⁷². Below 1 Hz, both attenuation mechanisms affect S waves significantly more strongly than P waves owing to the longer propagation time of S waves. From a single seismic record, one can isolate source effects by correcting the observed spectra for different values of intrinsic shear wave attenuation Q_μ until the P- and S-spectra match. Doing that, we find that the P- and S-wave spectra of LF events cannot be explained by effects of intrinsic attenuation alone, but show a strong source imprint. As an example, Fig. 4a shows the P-wave spectrum of the high-SNR event S0173a corrected for an average $Q_\mu = 1,000$, requiring a corner frequency $f_c = 0.45 \pm 0.15$ Hz.

Following refs. ^{38,73}, we assume that the source spectrum of a marsquake can be described by

$$A_{\text{src}}(f) = \frac{\Omega_0}{[1 + (f/f_c)^{vn}]^{1/v}}, \quad (3)$$

where Ω_0 is the amplitude at long period, describing the total deformation caused by the event. In the classical definition of Brune ³⁸, $v = 1$, $n = 2$. This fits the theoretical prediction of the Haskell source model of a single patch rupturing from one side to the other, while elongated faults lead to values of $n > 2$. The corner frequency f_c is related to the stress drop $\Delta\sigma$ by

$$f_c = k\beta^3 \sqrt{\frac{16}{7} \frac{\Delta\sigma}{M_0}}, \quad (4)$$

where β is the shear wave speed, M_0 is the scalar moment of the source and k is a dimensionless scaling parameter. For circular ruptures, it has been shown ⁷⁴ that $k = 0.38$ and 0.26 for P and S waves, respectively. All else being equal, we therefore expect the P- and S-wave spectra to be similar, with a corner frequency that is potentially higher for the P wave.

The measured displacement spectrum at the receiver $A(f)$ is further shaped by viscoelastic attenuation along the path, described by the intrinsic quality factor $Q(f)$

$$A(f) = A_{\text{src}}(f) \exp\left(-\pi \frac{fT}{Q(f)}\right) \Big|_{Q(f)=Q_0} = A_{\text{src}}(f) \exp(-\pi f t^*), \quad (5)$$

where T is the propagation time and t^* an attenuation operator that describes the integrated attenuation over the travel path. Q generally

depends on frequency, often expressed as $Q(f) = Q_0 f^\alpha$ with $\alpha \approx 0.2$ (ref. ⁷⁵). Over narrow frequency ranges, this effect however can be neglected and we assume a constant $Q(f) = Q_0$. For the bulk of the Earth, the shear wave attenuation Q_μ^{-1} is significantly higher than the bulk attenuation Q_κ^{-1} , so a typical assumption is $Q_\kappa = \infty$. For a Poisson solid ($\alpha/\beta = \sqrt{3}$), this means $Q_p = 9/4Q_\mu = 9/4Q_s$. If the P and the S waves travel the same path, the ratio of their travel times is $\sqrt{3}$, resulting in $t_p^* \approx t_s^*/4$.

A full attenuation model of the Martian mantle and lithosphere including scattering does not yet exist, but we can assume that all LF marsquakes located in the Cerberus Fossae are affected by the same attenuation structure. We therefore attempt to remove the effect of attenuation (equation (5)) by choosing a value for Q_μ that minimizes the difference between the P and S spectra for all LF marsquakes located in the Cerberus Fossae. Following ref. ¹⁹, we assume that the propagation path for HF events is shallow and different compared with the LF events and therefore a different average Q_μ applies. After selecting these values for attenuation, we expect to be left with a reasonable estimate of the pure source spectrum, from which we can infer the corner frequency, f_c . Given the low signal-to-noise ratio and limited bandwidth of the Martian data (Fig. 4), we assume for simplicity that the corner frequencies for P and S waves are identical. Further, we fix $v = 1$ and only try to match for f_c and n .

To summarize, we correct for attenuation using

$$A_S(f) = A_{0,S} \underbrace{\frac{1}{1 + (f/f_c)^n}}_{A_{\text{src},S}(f)} \underbrace{\exp\left(-\frac{\pi f T_S}{Q_S}\right)}_{A_{\text{att},S}(f)} \quad (6)$$

and

$$A_P(f) = \xi A_{\text{src},S}(f) A_{\text{att},S}^{-(1/4)}(f), \quad (7)$$

where ξ is the zero-frequency P/S ratio, which depends mainly on the focal mechanism and on the wave velocities at the source. Since it is a constant offset, we fix it such that the long-period part of the P and S spectra match here.

We compute the spectra of P and S waves from a 30 s time window starting 10 s before the respective MQS pick. The short time window is chosen to mitigate the effect of lithospheric scattering. An additional noise spectrum is computed from a 60 s time window before the event to select a suitable frequency window for each individual event. The matching between observed $A_{\text{src},P}(f)$ and equation (3) is done manually for each event. We find that a value of $Q_\mu = 1,000$, equivalent to $Q_p = 2,250$, produces a reasonable match between P- and S-wave spectra. This is not to be understood as a final value for the intrinsic attenuation of the mantle, but just as a value for which source effects can be studied reasonably well. Extended Data Figs. 6 and 7 show that the value of $Q \approx 400$ proposed in ref. ¹¹ cannot explain both P and S spectra well and must be seen as an ‘effective Q' , describing the spectral decay and thereby combining effects of source and structure (as written therein). The Supplementary Information contains figures of observed spectra and matching source functions for all the 12 events discussed in this Article. We manually match two corner frequencies f_c to each event, a reasonable maximum and minimum, with a fixed slope of $n = 2.5$. For the final dataset in Table 1 and Fig. 4, we add an additional 0.1 to the uncertainty to account for the limited SNR of all events.

Data availability

All InSight SEIS data used in this paper are available from the IPGP Data Center, IRIS-DMC and NASA PDS.

References

1. Knapmeyer, M. et al. Working models for spatial distribution and level of Mars' seismicity. *J. Geophys. Res. E Planets* **111**, 1–23 (2006).

2. Tanaka, K. L. et al. Geologic map of Mars: U.S. Geological Survey Scientific Investigations Map 3292. *US Geol. Surv. Geol. Investig.* <https://doi.org/10.3133/sim3292> (2014).
3. Lognonné, P. et al. SEIS: Insight's seismic experiment for internal structure of Mars. *Space Sci. Rev.* **215**, 12–12 (2019).
4. Banerdt, W. B. et al. Initial results from the InSight mission on Mars. *Nat. Geosci.* **13**, 183–189 (2020).
5. Golombek, M. P. et al. Geology of the InSight landing site on Mars. *Nat. Commun.* **11**, 1014 (2020).
6. Phillips, R. J. Expected Rate of Marsquakes. *LPI Tech. Rept.* **91-02**, 35–38 (Lunar and Planetary Institute, 1991).
7. Gudkova, T. V., Batov, A. V. & Zharkov, V. N. Model Estimates of non-hydrostatic stresses in the Martian crust and mantle: 1–Two-level model. *Sol. Syst. Res.* **51**, 457–478 (2017).
8. Berman, D. C. & Hartmann, W. K. Recent fluvial, volcanic, and tectonic activity on the Cerberus Plains of Mars. *Icarus* **159**, 1–17 (2002).
9. Anderson, R. C. et al. Primary centers and secondary concentrations of tectonic activity through time in the western hemisphere of Mars. *J. Geophys. Res. Planets* **106**, 20563–20585 (2001).
10. Lognonné, P. et al. Constraints on the shallow elastic and anelastic structure of Mars from InSight seismic data. *Nat. Geosci.* **13**, 213–220 (2020).
11. Giardini, D. et al. The seismicity of Mars. *Nat. Geosci.* **13**, 205–212 (2020).
12. Brinkman, N. et al. First focal mechanisms of marsquakes. *J. Geophys. Res. Planets* **126**, e2020JE006546 (2021).
13. Clinton, J. F. et al. The Marsquake catalogue from InSight, sols 0–478. *Phys. Earth Planet. Inter.* **310**, 106595 (2021).
14. InSight Marsquake Service (2022). Mars Seismic Catalogue, InSight Mission; V9 2022-01-01. ETHZ, IPGP, JPL, ICL, Univ. Bristol. <https://doi.org/10.12686/a14>
15. Savas, C. et al. The marsquake catalogue from InSight sols 0–1011. *Phys. Earth Planet. Inter.* **106943** <https://doi.org/10.1016/j.pepi.2022.106943> (2022)..
16. Jacob, A. et al. Seismic sources of InSight marsquakes and seismotectonic context of Elysium Planitia, Mars. *Tectonophysics* **873**, 229434 (2022).
17. Durán, C. et al. Seismology on Mars: an analysis of direct, reflected, and converted seismic body waves with implications for interior structure. *Phys. Earth Planet. Inter.* **325**, 106851 (2022).
18. Stähler, S. C. et al. Seismic detection of the martian core. *Science* **373**, 443–448 (2021).
19. van Driel, M. et al. High-frequency seismic events on Mars observed by InSight. *J. Geophys. Res. Planets* **126**, e2020JE006670 (2021).
20. Horleston, A. et al. The far side of Mars – two distant marsquakes detected by InSight. *Seism. Rec.* **2**, 88–99 (2022).
21. Perrin, C. et al. Geometry and segmentation of Cerberus Fossae, Mars: implications for marsquake properties. *J. Geophys. Res. Planets* **127**, e2021JE007118 (2022).
22. Rivas-Dorado, S., Ruiz, J. & Romeo, I. Giant dikes and dike-induced seismicity in a weak crust underneath Cerberus Fossae, Mars. *Earth Planet. Sci. Lett.* **594**, 117692 (2022).
23. Head, J. W. Generation of recent massive water floods at Cerberus Fossae, Mars by dike emplacement, cryospheric cracking, and confined aquifer groundwater release. *Geophys. Res. Lett.* **30**, 1577 (2003).
24. Burr, D. M. Recent aqueous floods from the Cerberus Fossae, Mars. *Geophys. Res. Lett.* **29**, 1013 (2002).
25. Taylor, J., Teanby, N. A. & Wookey, J. Estimates of seismic activity in the cerberus fossae region of mars. *J. Geophys. Res. E Planets* **118**, 2570–2581 (2013).
26. Voigt, J. R. C. & Hamilton, C. W. Investigating the volcanic versus aqueous origin of the surficial deposits in Eastern Elysium Planitia, Mars. *Icarus* **309**, 389–410 (2018).
27. Horvath, D. G., Moitra, P., Hamilton, C. W., Craddock, R. A. & Andrews-Hanna, J. C. Evidence for geologically recent explosive volcanism in Elysium Planitia, Mars. *Icarus* **365**, 114499 (2021).
28. Banerdt, W. B., Golombek, M. P. & Tanaka, K. L. Stress and tectonics on Mars. In *Mars*, 249–297 (1992).
29. Hauber, E., Brož, P., Jagert, F., Jodłowski, P. & Platz, T. Very recent and wide-spread basaltic volcanism on Mars. *Geophys. Res. Lett.* **38**, n/a–n/a (2011).
30. Plesa, A.-C., Wieczorek, M., Knapmeyer, M., Walterova, M. & Breuer, D. Interior Dynamics and Thermal Evolution of Mars a Geodynamic Perspective, in *Geophysical Exploration of the Solar System*, Vol. 63 of *Advances in Geophysics* (eds Schmelzbach, C. & Stähler, S.) p 179–230 (Elsevier, 2022).
31. Zenhäusern, G. et al. Low-frequency marsquakes and where to find them: back azimuth determination using a polarization analysis approach. *Bull. Seismol. Soc. Am.* **112**, 1787–1805 (2022).
32. Stähler, S. C., Khan, A., Drilleau, M., Duran, A. C. & Samuel, H. Interior models of Mars from inversion of seismic body waves doi:10.18715/IPGP.2021.kpmqrnz8 (2021).
33. Böse, M. et al. Magnitude scales for marsquakes calibrated from InSight data. *Bull. Seismol. Soc. Am.* <https://doi.org/10.1785/0120210045> (2021).
34. Knapmeyer, M. et al. Seasonal seismic activity on Mars. *Earth Planet. Sci. Lett.* **576**, 117171 (2021).
35. Knapmeyer, M. et al. Estimation of the seismic moment rate from an incomplete seismicity catalog, in the context of the InSight mission to Mars. *Bull. Seismol. Soc. Am.* **109**, 1125–1147 (2019).
36. Knapmeyer-Endrun, B. et al. Thickness and structure of the martian crust from InSight seismic data. *Science* **373**, 438–443 (2021).
37. Vetterlein, J. & Roberts, G. P. Structural evolution of the Northern Cerberus Fossae graben system, Elysium Planitia, Mars. *J. Struct. Geol.* **32**, 394–406 (2010).
38. Brune, J. N. Tectonic stress and the spectra of seismic shear waves from earthquakes. *J. Geophys. Res.* **1896–1977** **75**, 4997–5009 (1970).
39. Abercrombie, R. E. Earthquake source scaling relationships from -1 to 5 ML using seismograms recorded at 2.5-km depth. *J. Geophys. Res. Solid Earth* **100**, 24015–24036 (1995).
40. Allmann, B. P. & Shearer, P. M. Global variations of stress drop for moderate to large earthquakes. *J. Geophys. Res. Solid Earth* <https://doi.org/10.1029/2008JB005821> (2009).
41. Compaire, N. et al. Autocorrelation of the ground vibrations recorded by the SEIS-InSight seismometer on Mars. *J. Geophys. Res. Planets* **126**, e2020JE006498 (2021).
42. Laske, G., Masters, G., Ma, Z. & Pasyanos, M. Update on CRUST1.0 – A 1-degree global model of Earth's crust. *Geophys. Res. Abstracts* **15**, Abstract EGU2013-2658 (2013).
43. Drilleau, M. et al. Marsquake locations and 1-D seismic models for Mars from InSight data. *J. Geophys. Res. Planets* <https://doi.org/10.1002/essoar.10511074.2> (2022).
44. Abercrombie, R. E. Resolution and uncertainties in estimates of earthquake stress drop and energy release. *Philos. Trans. R. Soc. Math. Phys. Eng. Sci.* **379**, 20200131 (2021).
45. Giampiccolo, E., D'Amico, S., Patane, D. & Gresta, S. Attenuation and source parameters of shallow microearthquakes at Mt. Etna Volcano, Italy. *Bull. Seismol. Soc. Am.* **97**, 184–197 (2007).
46. Oberst, J. Unusually high stress drops associated with shallow moonquakes. *J. Geophys. Res.* **92**, 1397–1405 (1987).
47. Hensch, M. et al. Deep low-frequency earthquakes reveal ongoing magmatic recharge beneath Laacher See Volcano (Eifel, Germany). *Geophys. J. Int.* **216**, 2025–2036 (2019).

48. Chouet, B. A. & Matzoa, R. S. A multi-decadal view of seismic methods for detecting precursors of magma movement and eruption. *J. Volcanol. Geotherm. Res.* **252**, 108–175 (2013).
49. Kedar, S. et al. Analyzing low frequency seismic events at Cerberus Fossae as long period volcanic quakes. *J. Geophys. Res. Planets* **126**, e2020JE006518 (2021).
50. Madariaga, R. Dynamics of an expanding circular fault. *Bull. Seismol. Soc. Am.* **66**, 639–666 (1976).
51. Roberts, G. P., Matthews, B., Bristow, C., Guerrieri, L. & Vetterlein, J. Possible evidence of paleomarsquakes from fallen boulder populations, Cerberus Fossae, Mars. *J. Geophys. Res. Planets* **117**, n/a-n/a (2012).
52. Kolzenburg, S. et al. Solid as a rock: tectonic control of graben extension and dike propagation. *Geology* **50**, 260–265 (2021).
53. Watters, T. R. et al. Shallow seismic activity and young thrust faults on the Moon. *Nat. Geosci.* **12**, 411–417 (2019).
54. Plesa, A.-C. et al. Present-day Mars' seismicity predicted from 3-D thermal evolution models of interior dynamics. *Geophys. Res. Lett.* **45**, 2580–2589 (2018).
55. Bergman, E. A. Intraplate earthquakes and the state of stress in oceanic lithosphere. *Tectonophysics* **132**, 1–35 (1986).
56. Clauser, C. & Huenges, E. in *Thermal Conductivity of Rocks and Minerals* (ed Ahrens, T.) 105–126 (American Geophysical Union (AGU), 1995).
57. Khan, A. et al. Imaging the upper mantle structure of Mars with InSight seismic data. *Science* **373**, 434–438 (2021).
58. Byrne, P. K. A comparison of inner solar system volcanism. *Nat. Astron.* **4**, 321–327 (2020).
59. Clinton, J. F. et al. The Marsquake Service: securing daily analysis of SEIS data and building the martian seismicity catalogue for InSight. *Space Sci. Rev.* **214**, 133–133 (2018).
60. Böse, M. et al. A probabilistic framework for single-station location of seismicity on Earth and Mars. *Phys. Earth Planet. Inter.* **262**, 48–65 (2016).
61. Schimmel, M. & Gallart, J. The use of instantaneous polarization attributes for seismic signal detection and image enhancement. *Geophys. J. Int.* **155**, 653–668 (2003).
62. Ceylan, S. et al. Companion guide to the marsquake catalog from InSight, Sols 0–478: data content and non-seismic events. *Phys. Earth Planet. Inter.* **310**, 106597–106597 (2021).
63. Scholz, J.-R. et al. Detection, analysis, and removal of glitches from InSight's seismic data From Mars. *Earth Space Sci.* **7**, 1–31 (2020).
64. Kim, D. et al. Potential pitfalls in the analysis and structural interpretation of seismic data from the Mars InSight mission. *Bull. Seismol. Soc. Am.* **111**, 2982–3002 (2021).
65. VanDecar, J. C. & Crosson, R. S. Determination of teleseismic relative phase arrival times using multi-channel cross-correlation and least squares. *Bull. Seismol. Soc. Am.* **80**, 150–169 (1990).
66. Kim, D. et al. Improving constraints on planetary interiors with PPs receiver functions. *J. Geophys. Res. Planets* **126**, e2021JE006983 (2021).
67. Kagan, Y. Y. Seismic moment distribution revisited: I. Statistical results. *Geophys. J. Int.* **148**, 520–541 (2002).
68. Kane, D. L., Prieto, G., Vernon, F. L. & Shearer, P. M. Quantifying seismic source parameter uncertainties. *Bull. Seismol. Soc. Am.* **101**, 535–543 (2011).
69. Trugman, D. T., Dougherty, S. L., Cochran, E. S. & Shearer, P. M. Source spectral properties of small to moderate earthquakes in Southern Kansas. *J. Geophys. Res. Solid Earth* **122**, 8021–8034 (2017).
70. Aki, K. & Chouet, B. Origin of coda waves: source, attenuation, and scattering effects. *J. Geophys. Res.* **80**, 3322–3342 (1975).
71. Yoshimoto, K., Sato, H. & Otake, M. Frequency-dependent attenuation of P and S waves in the Kanto area, Japan, based on the coda-normalization method. *Geoph. J. Int.* **114**, 165–174 (1993).
72. Nakamura, Y. & Koyama, J. Seismic Q of the Lunar Upper Mantle. *J. Geophys. Res.* **87**, 4855–4861 (1982).
73. Boatwright, J. Seismic estimates of stress release. *J. Geophys. Res. Solid Earth* **89**, 6961–6968 (1984).
74. Kaneko, Y. & Shearer, P. M. Seismic source spectra and estimated stress drop derived from cohesive-zone models of circular subshear rupture. *Geoph. J. Int.* **197**, 1002–1015 (2014).
75. Baig, A. M., Dahlen, F. A. & Hung, S.-H. traveltimes of waves in three-dimensional random media. *Geophys. J. Int.* **153**, 467–482 (2003).
76. Smith, D. E. et al. Mars Orbiter Laser Altimeter: experiment summary after the first year of global mapping of Mars. *J. Geophys. Res. Planets* **106**, 23689–23722 (2001).
77. Dahmen, N. L. et al. Resonances and lander modes observed by InSight on Mars (1–9 Hz). *Bull. Seismol. Soc. Am.* **111**, 2924–2950 (2021).
78. Hobiger, M. et al. The shallow structure of Mars at the InSight landing site from inversion of ambient vibrations. *Nat Commun* **12**, 6756 (2021).
79. Iio, Y. Scaling relation between earthquake size and duration of faulting for shallow earthquakes in seismic moment between 10^{10} and 10^{25} dyne cm. *J. Phys. Earth* **34**, 127–169 (1986).
80. Bilek, S. L., Lay, T. & Ruff, L. J. Radiated seismic energy and earthquake source duration variations from teleseismic source time functions for shallow subduction zone thrust earthquakes. *J. Geophys. Res. Solid Earth* **109**, B09308 (2004).
81. Matsuzawa, T., Obara, K. & Maeda, T. Source duration of deep very low frequency earthquakes in western Shikoku, Japan. *J. Geophys. Res. Solid Earth* **114**, B00A11 (2009).
82. Prieto, G., Parker, R. L. & Vernon, F. L. A Fortran 90 library for multitaper spectrum analysis. *Comput. Geosci.* **35**, 1701–1710 (2009).

Acknowledgements

We acknowledge NASA, CNES, partner agencies and institutions (UKSA, SSO, DLR, JPL, IPGP-CNRS, ETHZ, IC and MPS-MPG), and the operators of JPL, SISMOC, MSDS, IRIS-DMC and PDS for providing SEED SEIS data. S.C.S. acknowledges funding from ETH research grant ETH-10 17-3. S.C.S., G.Z. and D.G. acknowledge support from ETHZ through the ETH+ funding scheme (ETH+2 19-1: 'Planet MARS'). Marsquake Service (MQS) operations at ETH are supported by ETH Research grant ETH-06 17-02. A.M. acknowledges support from ETH 19-2 FEL-34 and the Harvard Daly Postdoctoral Fellowship. C.P. acknowledges support from CNES as well as Agence Nationale de la Recherche (ANR-14-CE36-0012-02 and ANR-19-CE31-0008-08). W.B.B. was supported by the NASA InSight mission and funds from the Jet Propulsion Laboratory, California Institute of Technology, under a contract with the National Aeronautics and Space Administration (80NM0018D0004). This is InSight contribution 233.

Author contributions

S.C.S. designed the study with contributions from all authors. A.M. and C.P. led the geological context analysis. S.C.S., T.K. and P.L. analysed the waveform spectra. M.K. and S.C.S. analysed the seismic moment release. J.C., S.C.S. and D.G. reviewed the MQS analysis on event distances. G.Z., J.C. and S.C.S. analysed LF event back azimuths. D.K. added the analysis of the HF event back azimuth. D.G., P.L. and W.B.B. designed the InSight seismic experiment. S.C.S. and A.M. wrote the paper with help from all authors.

Competing interests

The authors declare no competing interests.

Additional information

Extended data is available for this paper at
<https://doi.org/10.1038/s41550-022-01803-y>.

Supplementary information The online version contains supplementary material available at
<https://doi.org/10.1038/s41550-022-01803-y>.

Correspondence and requests for materials should be addressed to Simon C. Stähler.

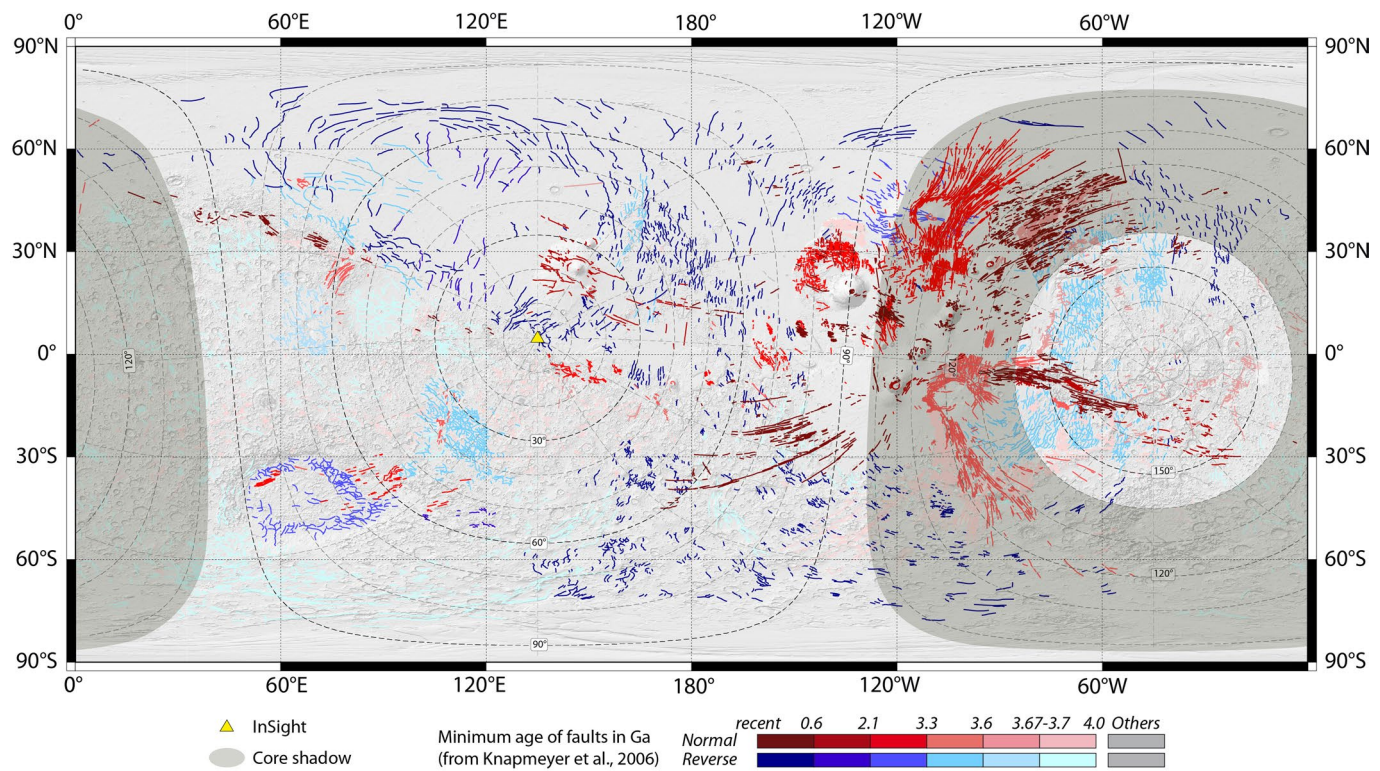
Peer review information *Nature Astronomy* thanks Ernst Hauber, Gerald Roberts and the other, anonymous, reviewer(s) for their contribution to the peer review of this work.

Reprints and permissions information is available at
www.nature.com/reprints.

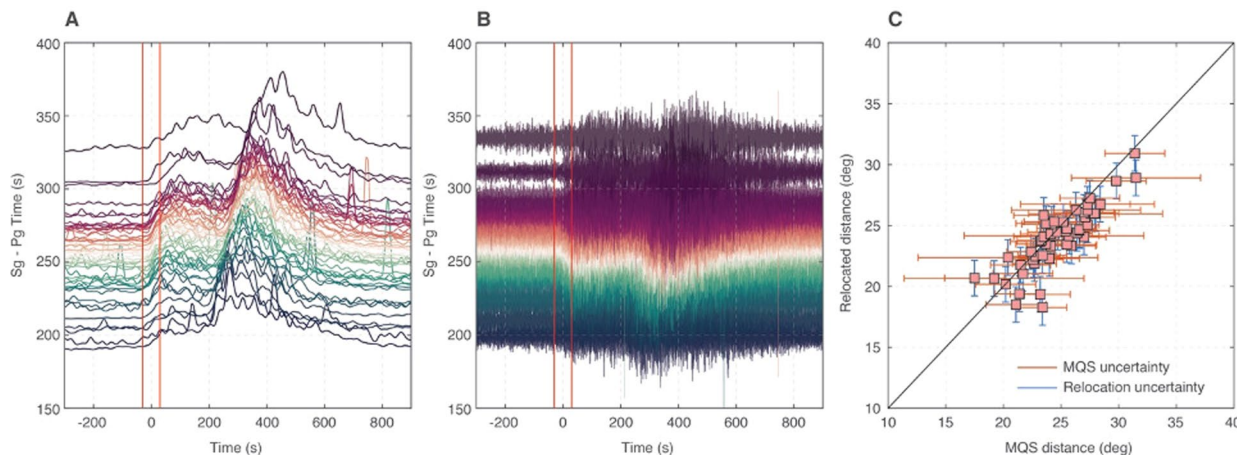
Publisher's note Springer Nature remains neutral with regard to jurisdictional claims in published maps and institutional affiliations.

Springer Nature or its licensor (e.g. a society or other partner) holds exclusive rights to this article under a publishing agreement with the author(s) or other rightholder(s); author self-archiving of the accepted manuscript version of this article is solely governed by the terms of such publishing agreement and applicable law.

© The Author(s), under exclusive licence to Springer Nature Limited 2022

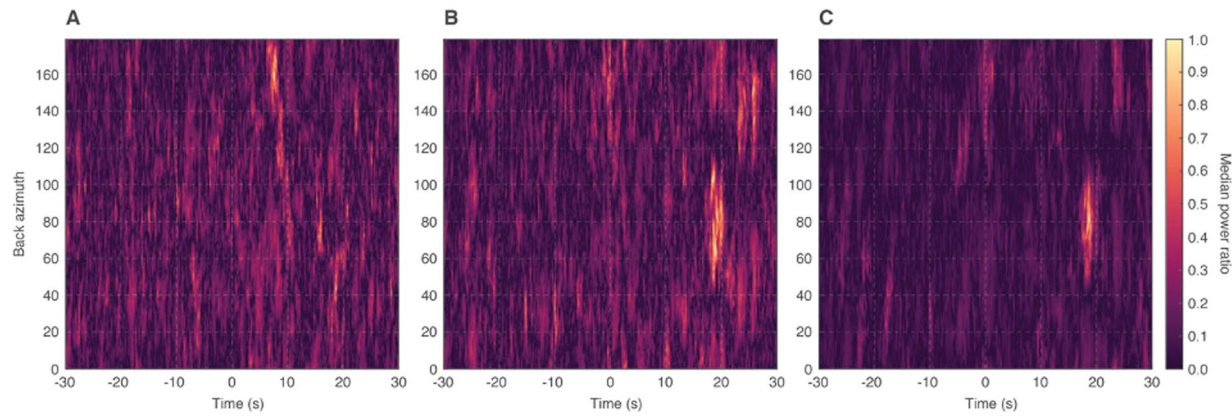


Extended Data Fig. 1 | Global fault map. Global map of faults color-coded by minimum age^{1,2,76}. The darkened area marks the core shadow¹⁸, in which no direct body waves can be observed as seen from InSight. Thus event detection is significantly more difficult.


Extended Data Fig. 2 | Realignment of HF marsquake arrival times.

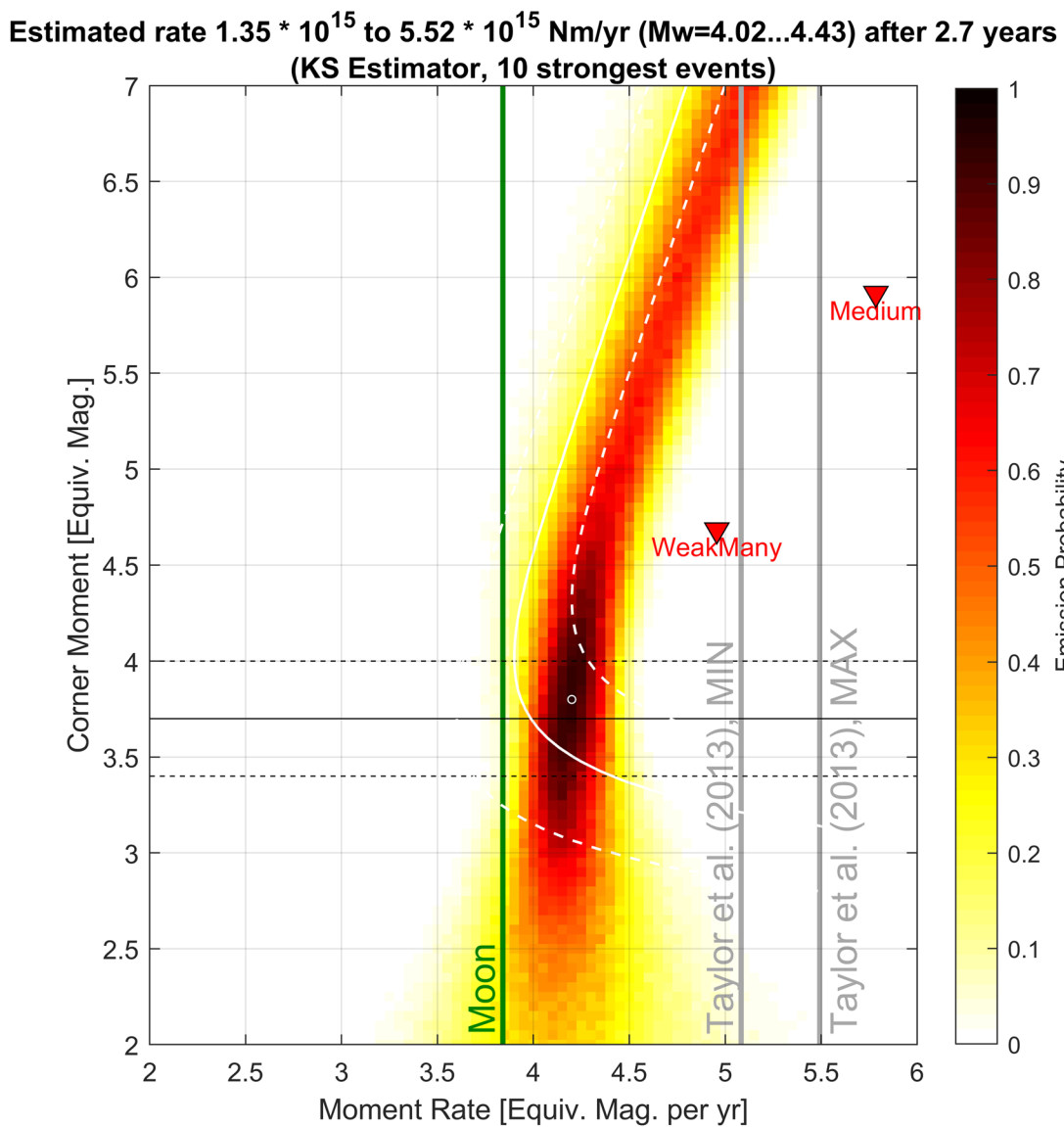
(A) Average three-component envelopes aligned on Pg-arrival ($t = 0$ s) from a total of 62 marsquakes from the HF event category, and the corresponding (B) vertical component waveforms. All MQS events with the event quality C or above are

selected between Sols 128 and 1050¹⁴ but those with low envelope similarity (that is, correlation coefficient < 0.8 against the mean envelope of all HF event data) are removed. (C) Comparison of the MQS vs. relocated distance estimates with $v_{Pg}=4$ km/s and $v_{Pg}/v_{Sg}=\sqrt{3}$, including standard deviation.



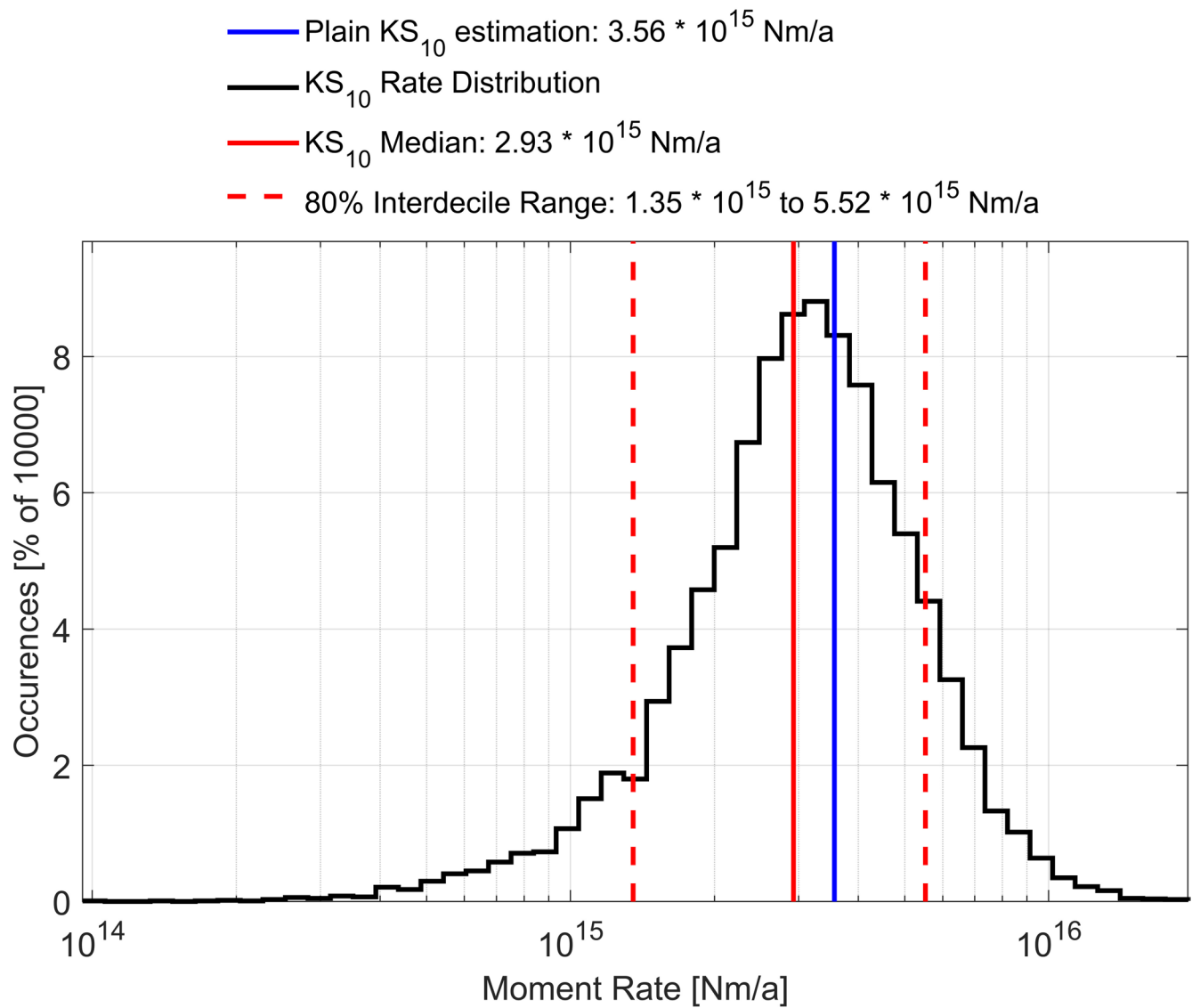
Extended Data Fig. 3 | Backazimuth estimation from radial vs transverse energy. Median power ratio between radial and transverse components of the HF waveforms (A) before, and (B) after applying the re-alignment using average

spectral envelopes. (C) Same as (B) but using a subgroup of HF events that clustered tightly at the mean relocated distance of 24°. Background power which is strongly affected by wind noise and lander resonances is removed.

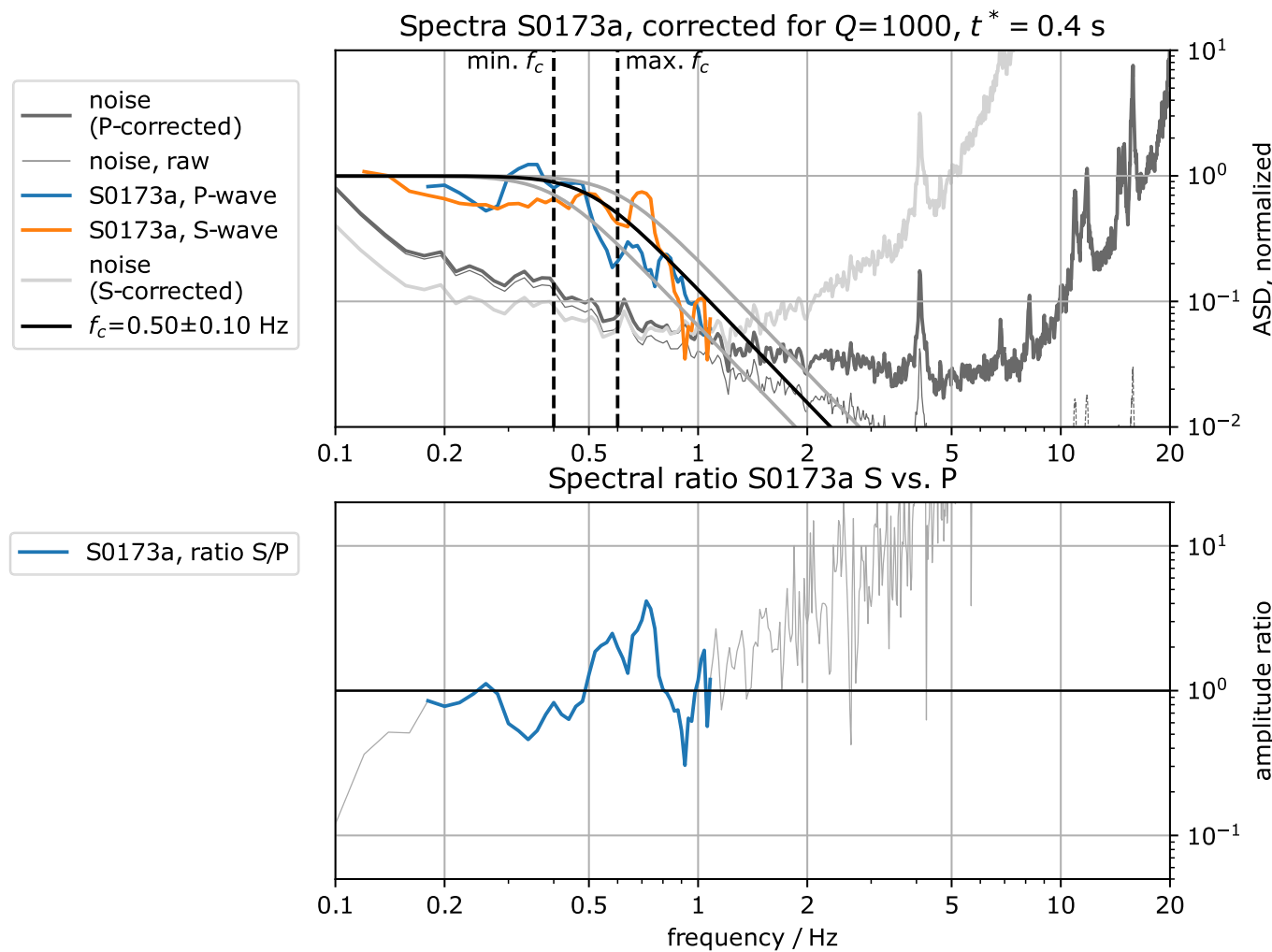


Extended Data Fig. 4 | Probability of moment rate and corner magnitude in Cerberus Fossae. Emission probability of moment rate and corner moment taking into account the 10 largest events observed over the mission until 2021-12-31, using the KS10 estimator of³⁵, in the same style as figs. 4, 7 therein. For

orientation, the moment release of the whole moon, as seen by the Apollo seismic network over 7 years of operation⁴⁶ (green) and the moment rates estimated by²⁵ for Cerberus Fossae (grey) are shown, as well as 2 global estimates from¹ (Many weak faults and the medium model).

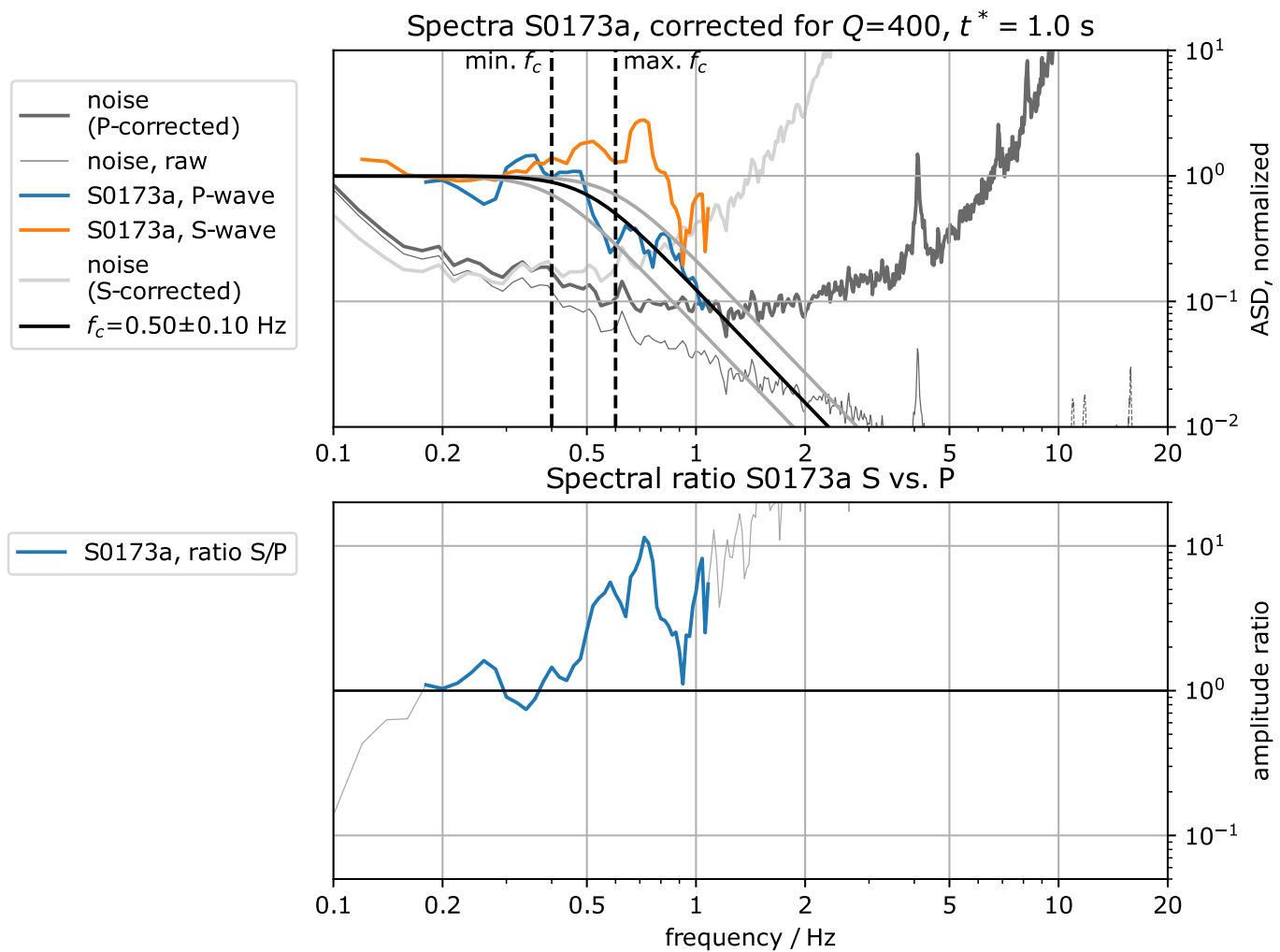


Extended Data Fig. 5 | Probability distribution of annual moment rate. Distribution of annual moment release rate \dot{M} resulting from the emission probability in Extended Data Figure 4.

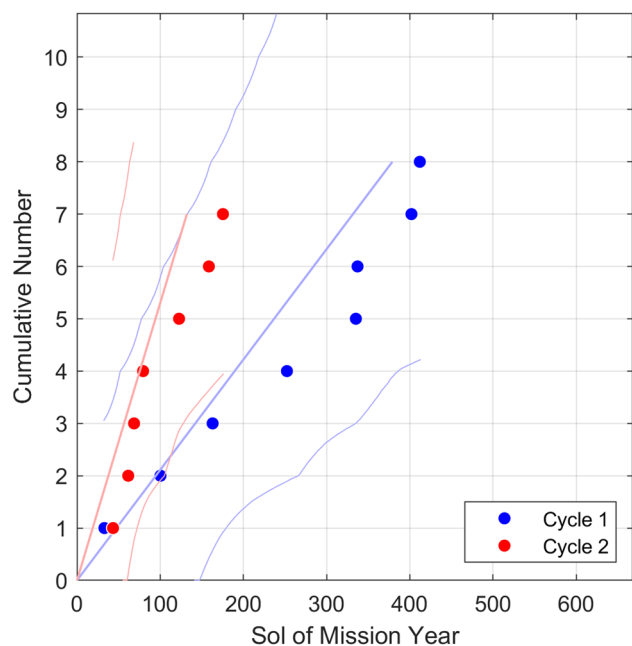


Extended Data Fig. 6 | Spectral fit of marsquake S0173a. Spectral fitting example: Event S0173a, after correction for Q_μ (eq. (6), (7)). Top: The value of $Q_\mu = 1000$ has been chosen to make P and S-wave spectra match. Each spectrum was computed in a time window of 30 second length around the arrival using a multitaper method⁸². The S-wave and P-wave amplitude spectra meet the

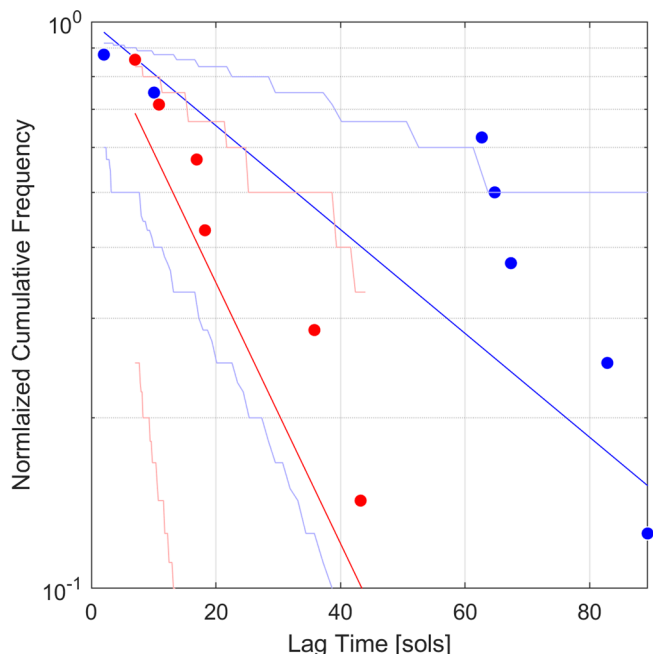
pre-event noise at 1.1 Hz. For easier comparison, the noise spectra are plotted 3 times: (i) raw, and using the correction terms for (ii) P- and (iii) S-waves. Bottom: Ratio of P- and S-wave spectrum. The colored part highlights the frequency range in which both P- and S-wave are above noise. The black line marks a theoretical spectrum (eq. (3)) with $f_c = 0.5$ Hz and $n = 2$.



Extended Data Fig. 7 | Spectral fit of marsquake S0173a with different attenuation model. Event S0173a, with the attenuation model of¹¹. The value of $Q_\mu = 400$ leads to a significant over-prediction of the S-wave amplitude above 0.5 Hz.


Extended Data Fig. 8 | Test for Poissonian distribution of marsquakes.

Cumulative count of events (left), and lag time distribution (right). For a stationary Poisson process, the cumulative count as function of time should follow a straight line in linear coordinates. The event rate defines the slope of this line. For the first year of operation (cycle 1, blue), we corrected the count after the three weeks down time in August/September 2019 by assuming that the rate during the down time equalled that afterwards. After Sol 400, increasing wind speeds at night made detection impossible until the second Martian year, starting around Sol 700. For the second year (cycle 2), no such correction was



necessary. Pale lines indicate the nominal slope (cycle 1: 0.021 ± 0.007 events/sol, cycle 2: 0.053 ± 0.02 events/sol) and the 95% confidence intervals for likely scatter. The event series end with the end of the catalog (MQS v9). The lag times of a stationary Poisson process are exponentially distributed and thus follow a straight line in a semi-logarithmic plot. Lag times shorter than 1 sol were not considered; the daily noise regime makes them unreliable. All confidence intervals estimated numerically from 1e5 synthetic event sequences with the same rate and covering the same duration.